

Key Points:

- Tsunamis were accurately predicted using well-mapped outer-rise normal faults along the Japan Trench
- It is necessary to carefully select the earthquake scaling law when predicting tsunamis from outer-rise earthquakes.
- Heterogeneous slips have a large impact on tsunami predictions for outer-rise earthquakes.

Supporting Information:

- Supporting Information S1

Correspondence to:

T. Baba,
 baba.toshi@tokushima-u.ac.jp

Citation:

Baba, T., Chikadasa, N., Nakamura, Y., Fujie, G., Obana, K., Miura, S., & Kodaira, S. (2020). Deep investigations of outer-rise tsunami characteristics using well-mapped normal faults along the Japan Trench. *Journal of Geophysical Research: Solid Earth*, 125, e2020JB020060. <https://doi.org/10.1029/2020JB020060>

Received 24 APR 2020

Accepted 16 SEP 2020

Accepted article online 17 SEP 2020

©2020. The Authors.

This is an open access article under the terms of the Creative Commons Attribution License, which permits use, distribution and reproduction in any medium, provided the original work is properly cited.

Deep Investigations of Outer-Rise Tsunami Characteristics Using Well-Mapped Normal Faults Along the Japan Trench

Toshitaka Baba¹ , Naotaka Chikadasa² , Yasuyuki Nakamura³, Gou Fujie³ , Koichiro Obana³, Seiichi Miura³, and Shuichi Kodaira³ 

¹Graduate School of Science and Technology, Tokushima University, Tokushima, Japan, ²National Research Institute for Earth Science and Disaster Resilience, Ibaraki, Japan, ³Research and Development Center for Earthquake and Tsunami, Japan Agency for Marine-Earth Science and Technology, Yokohama, Japan

Abstract To assess the risk of tsunamis from outer-rise earthquakes, we carried out tsunami simulations using 33 simple rectangular fault models with 60° dip angles based on marine seismic observations and surveys of the Japan Trench. The largest tsunami resulting from these models, produced by a M_w 8.7 normal-faulting event on a fault 332 km long, had a maximum height of 27.0 m. We tested variations of the predictions due to the uncertainties in the assumed parameters. Because the actual dip angles of the Japan Trench outer-rise faults range from 45° to 75°, we calculated tsunamis from earthquakes on fault models with 45°, 60°, and 75° dip angles. We also tested a compound fault model with 75° dip in the upper half and 45° dip in the lower half. Rake angles were varied by $\pm 15^\circ$. We also tested models consisting of small subfaults with dimensions of about 60 km, models using other earthquake scaling laws, models with heterogeneous slips, and models incorporating dispersive tsunami effects. Predicted tsunami heights changed by 10–15% for heterogeneous slips, up to 10% for varying dip angles, about 5–10% from considering tsunami dispersion, about 2% from varying rake angles, and about 1% from using the model with small subfaults. The use of different earthquake scaling laws changed predicted tsunami heights by about 50% on average for the 33 fault models. We emphasize that the earthquake scaling law used in tsunami predictions for outer-rise earthquakes should be chosen with great care.

1. Introduction

Outer-rise earthquakes occur as a result of the bending of the subducting plate on the seaward side of the trench axis, and many have been documented in connection with great interplate earthquakes. A famous example is the 1933 Showa-Sanriku outer-rise earthquake ($M8.4$, Abe, 1978; Kanamori, 1971; Uchida et al., 2016), which followed the 1896 Meiji-Sanriku interplate earthquake ($M8.2$, Tanioka & Satake, 1996a). Tsunamis generated by both events caused significant damage along the coast of northeastern Japan. More recently, the 2006 Kuril interplate earthquake ($M8.3$) was followed by the 2007 Kuril outer-rise earthquake ($M8.1$) two months later (Ammon et al., 2008; Baba et al., 2009; Fujii & Satake, 2008; Lay et al., 2009), and the 2009 Samoa-Tonga outer-rise earthquake occurred almost simultaneously with two interplate earthquakes (both $M7.8$) (Lay et al., 2010; Okal et al., 2010). The time difference between interplate and outer-rise earthquakes varies, but the two events have similar magnitudes. In Japan, the giant Tohoku interplate earthquake ($M9.0$) occurred on 11 March 2011, but a corresponding outer-rise earthquake has not yet occurred. It is a concern that one will occur, perhaps shortly.

To improve early warning of shaking and tsunamis due to offshore earthquakes, a large-scale cabled observatory, the Seafloor Observation Network for Earthquakes and Tsunamis along the Japan Trench (S-net) was deployed in 2011 (NIED, 2019). S-net is equipped with about 150 ocean-bottom pressure gauges that can register the passage of tsunamis before their arrival at the coast and seven GPS-equipped buoys that can measure changes in sea level (Kato et al., 2005) have been installed less than 20 km off the coast. Real-time tsunami prediction systems have been developed that rely on offshore tsunami observation data. The tFISH method (Tsushima et al., 2009, 2012) estimates the initial sea surface deformation by inverting pressure data in real time. Maeda et al. (2015) and Wang et al. (2017) have applied data assimilation techniques to the pressure data to improve predictions of tsunami propagation.

Yamamoto et al. (2016) have created a precomputed database that includes tsunami scenarios in the Japan Trench, from which an optimal scenario is chosen to match the maximum tsunami heights observed by S-net. Regression models between offshore and coastal tsunamis based on that tsunami database have been constructed by Baba et al. (2014) and Igarashi et al. (2016). Almost all tsunami early warning systems currently in operation use precomputed tsunami databases. The Japan Meteorological Agency's tsunami database includes 100,000 tsunami scenarios. The Joint Australian Tsunami Warning Centre (Greenslade et al., 2011, 2014) and the Indian Ocean tsunami early warning center (Nayak & Kumar, 2008a, 2008b) also use precomputed databases when issuing warnings. Turkey's tsunami warning system for the Mediterranean and Marmara Seas searches tsunami databases to find the scenario that best fits the observed data (Necmioğlu & Özel, 2014). The construction of tsunami databases starts by compiling a database of faults that could generate tsunamis. We concern characteristics of outer-rise faults in the Japan Trench for tsunami predictions.

Investigations of the incoming plate at the Japan Trench have been conducted in an area from 36.5°N to 40.5°N to clarify the properties of outer-rise earthquakes (Fujie et al., 2016; Obana et al., 2012, 2018, 2019). Bending plate outboard of subduction zones acquires a characteristic horst-and-graben topography, which can be interpreted as the cumulative displacement of multiple outer-rise earthquakes that took place in the past. For that reason, Kodaira et al. (2019) surveyed the seafloor topography in detail to create a red relief image map (Chiba et al., 2008) that emphasizes the undulations on the seafloor. In addition, multi-channel seismic reflection and passive-source seismic surveys were used to verify the lateral and vertical continuity of outer-rise faults. The distribution of earthquake hypocenters and focal mechanisms indicated that these fault planes had dip angles ranging from 45° to 75° and that the extensional stress field that causes normal fault earthquakes extends to a depth of about 40 km. This work led to a compilation of 33 candidate faults that might cause outer-rise earthquakes in the Japan Trench (Kodaira et al., 2019).

In this study, we predicted tsunamis on the basis of numerical simulations from the set of 33 faults. Section 2 of this paper describes how we validated the numerical procedures for our tsunami calculations by comparing predictions to observations of the tsunami from the 2010 Bonin earthquake, an outer-rise $M7.3$ earthquake in the Izu-Bonin Trench, made by a tide gauge and several DART stations. Section 3 describes our forward modeling of tsunamis at the Japan Trench using the validated procedure. Because actual earthquakes do not exactly match the assumed fault parameters, we conducted a sensitivity analysis to explore the effects of uncertainties in the assumed fault parameters, using the reliability indicators of Aida (1978). We focused in particular on the effects on tsunami propagation of uncertainties in dip angle and rake angle of the faults, the scaling law used to determine slip amounts, wave dispersion, and slip heterogeneity. In section 4, we discuss points to be aware of in making tsunami predictions for outer-rise earthquakes.

2. Model Validation Using the 2010 Bonin Tsunami

2.1. The 2010 Bonin Earthquake and Tsunami

On 21 December 2010 at 17:20 UTC, a normal-faulting earthquake occurred about 150 km east of the Bonin Islands, an outer-rise event in the Pacific plate (Figure 1). The U.S. Geological Survey (2010) estimated a seismic moment of 1.113×10^{20} Nm, a corresponding magnitude of M_w 7.3, and a centroid depth of 25.5 km. The causative fault plane had a dip angle of 46°, a strike angle of 113°, and a rake angle of -113° . Tsunami waves were observed at tide gauges in Japan and ocean-bottom pressure gauges of the DART system. A tsunami with a maximum height of 22 cm was recorded by the tide gauge at Chichijima, an island about 150 km from the epicenter. Tsunamis several centimeters high were recorded by DART Stations 21413, 52402, and 52405 in the Pacific Ocean. We used the data from this tsunami to validate our model for tsunami predictions from outer-rise earthquakes.

2.2. Tsunami Calculation Method

We used the U.S. Geological Survey parameters for the fault plane of the 2010 Bonin earthquake. Under our assumption that recurring outer-rise earthquakes developed the horst-and-graben seafloor topography, we set the upper edge of the fault plane at a very shallow depth (0.1 km) below the seafloor. From the moment magnitude and the scaling law proposed by the Álvarez-Gómez et al. (2012) for outer-rise earthquakes ($M = 3.89 + 1.89 \log_{10} L$), we obtained a fault length L of 64 km, and we assigned the fault plane a width W of 56 km based on the depth of the bottom of the seismogenic zone. The slip amount of the fault was calculated from the seismic moment, the values of L and W , and an assumed rigidity of 5.0×10^{10} N/m².

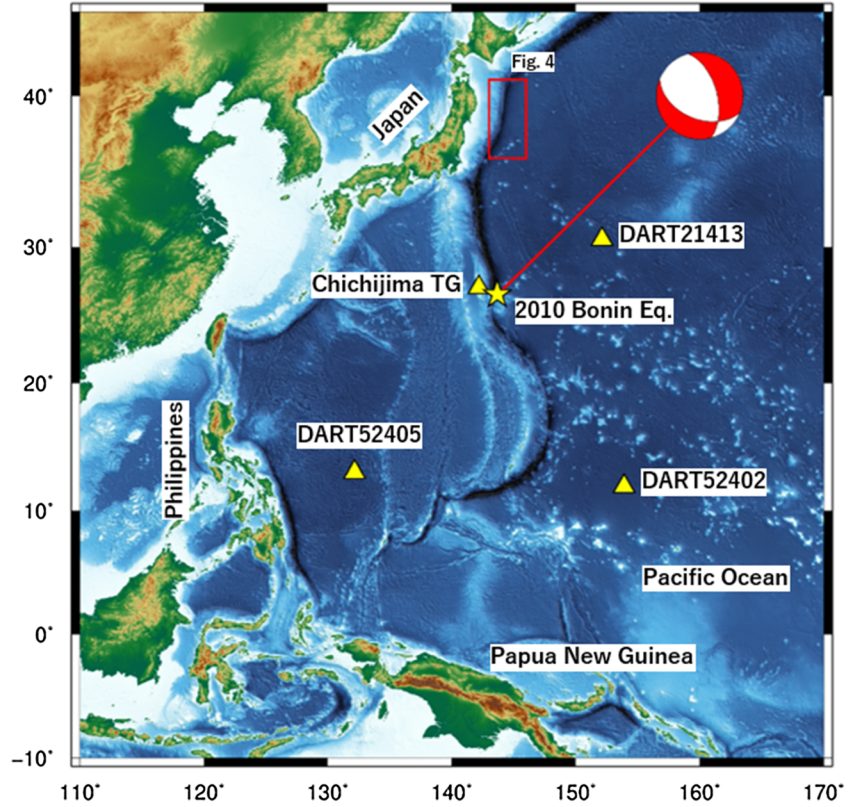


Figure 1. Location map showing the topography and bathymetry of the computational area for modeling the tsunami caused by the 2010 Bonin earthquake (star). Triangles indicate locations of the Chichijima tide gauge (TG) and three ocean-bottom pressure gauges of the DART system. The red outline encloses the region of the Japan Trench shown in Figure 4.

Vertical crustal displacement at the seafloor was calculated with the assumption that the crust is a homogeneous elastic half-space (Okada, 1985), and horizontal movement effects were included (Tanioka & Satake, 1996b). A hydraulic filter based on linear potential theory (Kajiura, 1963) was applied to estimate the initial sea surface displacement. The initial sea surface displacement assumed a rise time of 15 s because the moment release of the 2010 Bonin earthquake was finished by about 15 s. To model tsunami propagation, we used the nonlinear longwave (nondispersive) equations:

$$\frac{\partial U}{\partial t} + \frac{1}{R \sin \theta} \frac{\partial}{\partial \varphi} \left(\frac{U^2}{H + \eta} \right) + \frac{1}{R} \frac{\partial}{\partial \theta} \left(\frac{UV}{H + \eta} \right) = -g \frac{H + \eta}{R \sin \theta} \frac{\partial \eta}{\partial \varphi} - fV - \frac{gn^2}{(H + \eta)^{7/3}} U \sqrt{U^2 + V^2}, \quad (1)$$

$$\frac{\partial V}{\partial t} + \frac{1}{R \sin \theta} \frac{\partial}{\partial \varphi} \left(\frac{UV}{H + \eta} \right) + \frac{1}{R} \frac{\partial}{\partial \theta} \left(\frac{V^2}{H + \eta} \right) = -g \frac{H + \eta}{R} \frac{\partial \eta}{\partial \theta} + fU - \frac{gn^2}{(H + \eta)^{7/3}} V \sqrt{U^2 + V^2}, \quad (2)$$

$$\frac{\partial \eta}{\partial t} = -\frac{1}{R \sin \theta} \left(\frac{\partial U}{\partial \varphi} + \frac{\partial V \sin \theta}{\partial \theta} \right), \quad (3)$$

where U and V are the depth-integrated flow quantities equal to $(H + \eta)u$ and $(H + \eta)v$, respectively, along the φ (longitude) and θ (colatitude) directions, u and v are the corresponding horizontal flow velocities, H is the depth of the ocean at rest, R is the Earth's radius, t is time, η is the difference in sea level at time t from its value at rest, and g is the gravitational acceleration. The second and third terms on the right-hand side are the Coriolis and bottom friction forces, respectively, where f is the Coriolis parameter and n is Manning's roughness coefficient. The time integrations were solved by a leapfrog, staggered grid, finite-difference method using JAGURS open-source software (Baba et al., 2015, 2017). The advection terms (second and third terms on the left-hand side) were approximated by upwind difference to enhance stabilities during the calculations.

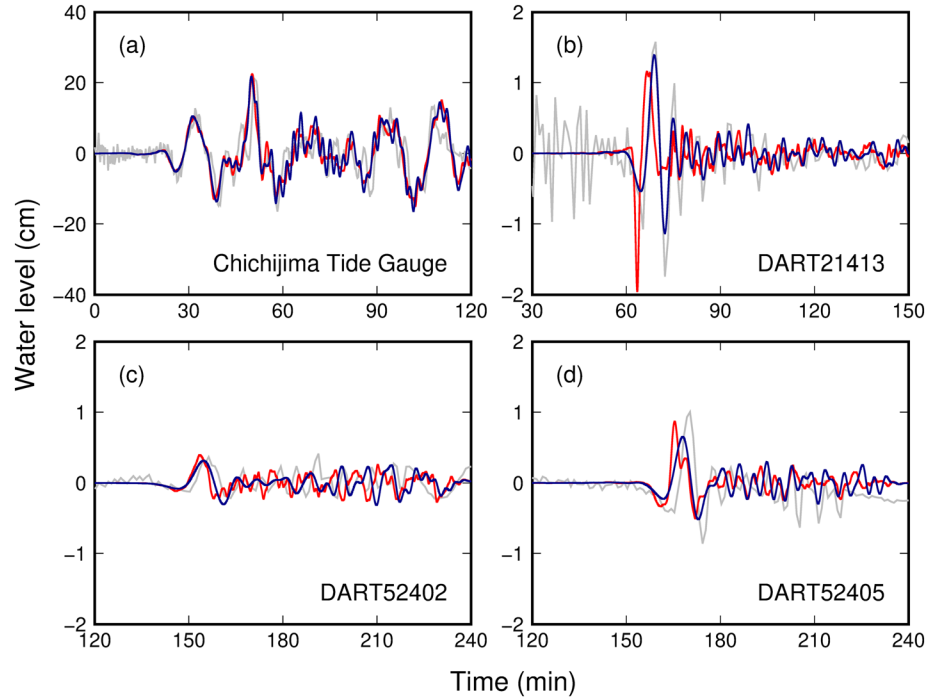


Figure 2. Waveforms of the 2010 Bonin tsunami obtained from observations (gray), nondispersive equations (red) and dispersive equations (blue). Note the difference in vertical scales.

We derived 30 arc sec gridded bathymetric data for the tsunami calculation area (Figure 1) from the General Bathymetric Chart of the Oceans (GEBCO_2014 Grid). Because tsunamis are sensitive to the shallow near-coast bathymetry and the shape of the coastline, the area around the Chichijima tide gauge was treated as a different domain with a 10/3 arc sec grid using more detailed M7000 series data (M7023) provided by the Japan Hydrographic Association (2017) and elevation data from the Geospatial Information Agency of Japan (GSI). For the nesting algorithm, an intermediate domain with a 10 arc sec grid was inserted between these domains. The outer boundary of the model was given a transmission boundary condition. The size of the time step width was set to be 0.4 s to satisfy the stability conditions of the finite difference calculation. Time series of water level changes were recorded at the locations of the tide gauge and DART stations (Figure 1). The observed and calculated tsunamis are compared in Figure 2.

Outer-rise earthquakes occur on steeply dipping faults, generating tsunamis with relatively short wavelengths. In gravity wave theory, dispersion effects are stronger at shorter wavelengths, and many studies have indicated that dispersive effects are not negligible for tsunamis caused by outer-rise earthquakes (Tanioka et al., 2018; Zhou et al., 2012). Accordingly, we also performed tsunami calculations using the dispersive equations in JAGURS software:

$$\begin{aligned} \frac{\partial U}{\partial t} + \frac{1}{R \sin \theta} \frac{\partial}{\partial \varphi} \left(\frac{U^2}{H + \eta} \right) + \frac{1}{R} \frac{\partial}{\partial \theta} \left(\frac{UV}{H + \eta} \right) & \quad (4) \\ = -g \frac{H + \eta}{R \sin \theta} \frac{\partial \eta}{\partial \varphi} - fV - \frac{gn^2}{(H + \eta)^{7/3}} U \sqrt{U^2 + V^2} + \frac{H^2}{3R \sin \theta} \frac{\partial}{\partial \varphi} \left[\frac{1}{R \sin \theta} \left(\frac{\partial^2 U}{\partial \varphi \partial t} + \frac{\partial^2 V \sin \theta}{\partial \theta \partial t} \right) \right], \end{aligned}$$

$$\begin{aligned} \frac{\partial V}{\partial t} + \frac{1}{R \sin \theta} \frac{\partial}{\partial \varphi} \left(\frac{UV}{H + \eta} \right) + \frac{1}{R} \frac{\partial}{\partial \theta} \left(\frac{V^2}{H + \eta} \right) & \quad (5) \\ = -g \frac{H + \eta}{R} \frac{\partial \eta}{\partial \theta} + fU - \frac{gn^2}{(H + \eta)^{7/3}} U \sqrt{U^2 + V^2} + \frac{H^2}{3R} \frac{\partial}{\partial \theta} \left[\frac{1}{R \sin \theta} \left(\frac{\partial^2 U}{\partial \varphi \partial t} + \frac{\partial^2 V \sin \theta}{\partial \theta \partial t} \right) \right], \end{aligned}$$

where the final terms on the right-hand side are the dispersion (Boussinesq) terms (Peregrine, 1972). The resulting tsunami waveforms are also shown in Figure 2.

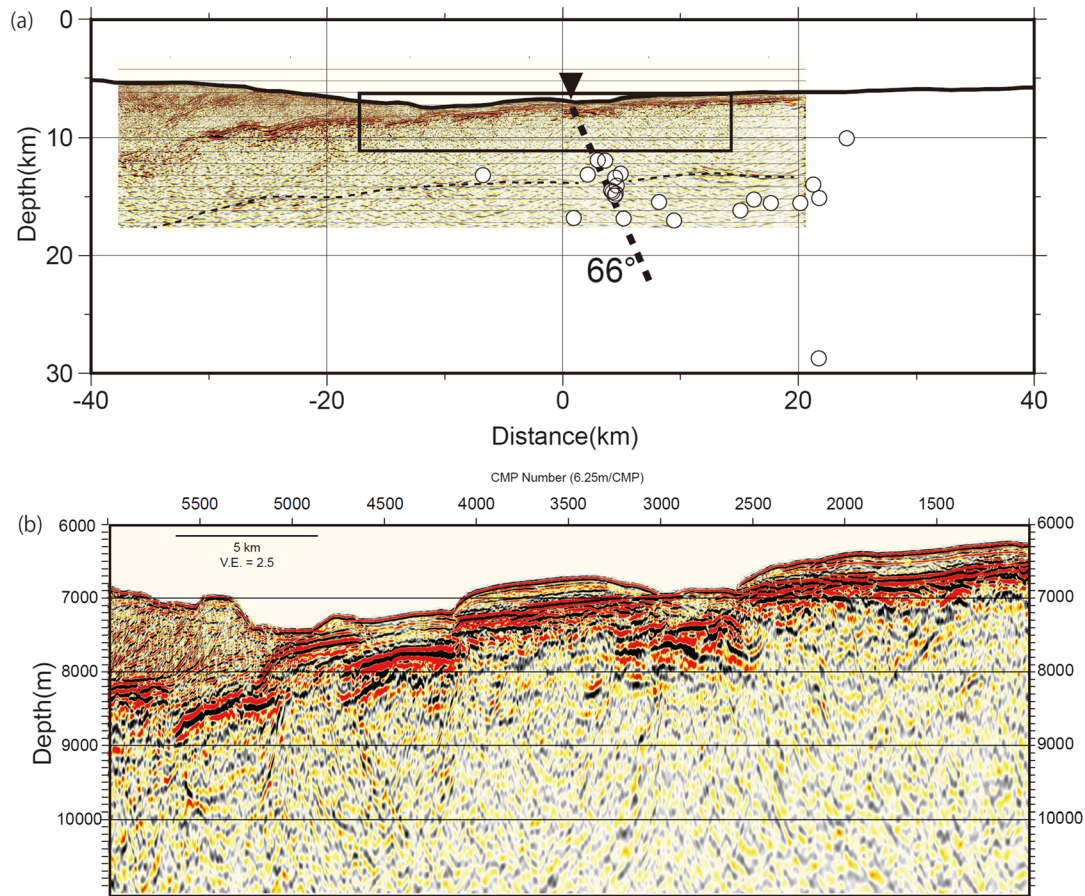


Figure 3. (a) A seismic reflection profile off the central section of the Japan Trench (D2 from Kodaira et al., 2017) plotted with hypocenters within 5 km of the profile (Obana et al., 2018). Location of the profile is shown in Figure 4. (b) Enlarged section of the rectangular area in (a).

2.3. Tsunami Calculation Results

In general, coastal tsunamis have complex patterns due to nonlinearity, shoaling effects, reflections, and refractions. Fortunately, the tsunami recorded at the Chichijima tide gauge was well modeled, not only for the leading wave but also for the later waves (Figure 2a). There was almost no difference between the calculated nondispersive and dispersive waveforms. However, the nondispersive and dispersive waveforms differed notably at each of the three DART stations. Including dispersive terms improved the reproducibility of the observed tsunami waveforms, especially for DART21413 (Figure 2b), but for DART21413 and DART52405, the maximum amplitudes of the calculated tsunamis were slightly smaller than those of the observed waves. We calculated the 2010 Bonin tsunami in a completely forward way, relying on only the seismic parameters. The quality of our predicted tsunami waveforms, except for the maximum amplitudes at some stations, indicates that our procedures are reasonable for predicting tsunamis from outer-rise earthquakes.

3. Tsunami Prediction for Outer-Rise Earthquakes in the Japan Trench

3.1. Setting of Basic Faults

Intensive marine surveys were carried out in the outer-rise area of the Japan Trench region from 2013 to 2018 (Figure 3). Results from seafloor topographic surveys, crustal structure surveys, and passive seismic monitoring have been published by Boston et al. (2014), Obana et al. (2018, 2019), Fujie et al. (2016, 2020), and Kodaira et al. (2017, 2019). The important findings of the surveys are these: (1) The upper edges of outer-rise faults are consistent with the horst-and-graben topography at the seafloor; (2) dip angles of these faults are steep, reaching a maximum of 75° at shallow subseafloor depths; (3) dip angles are more

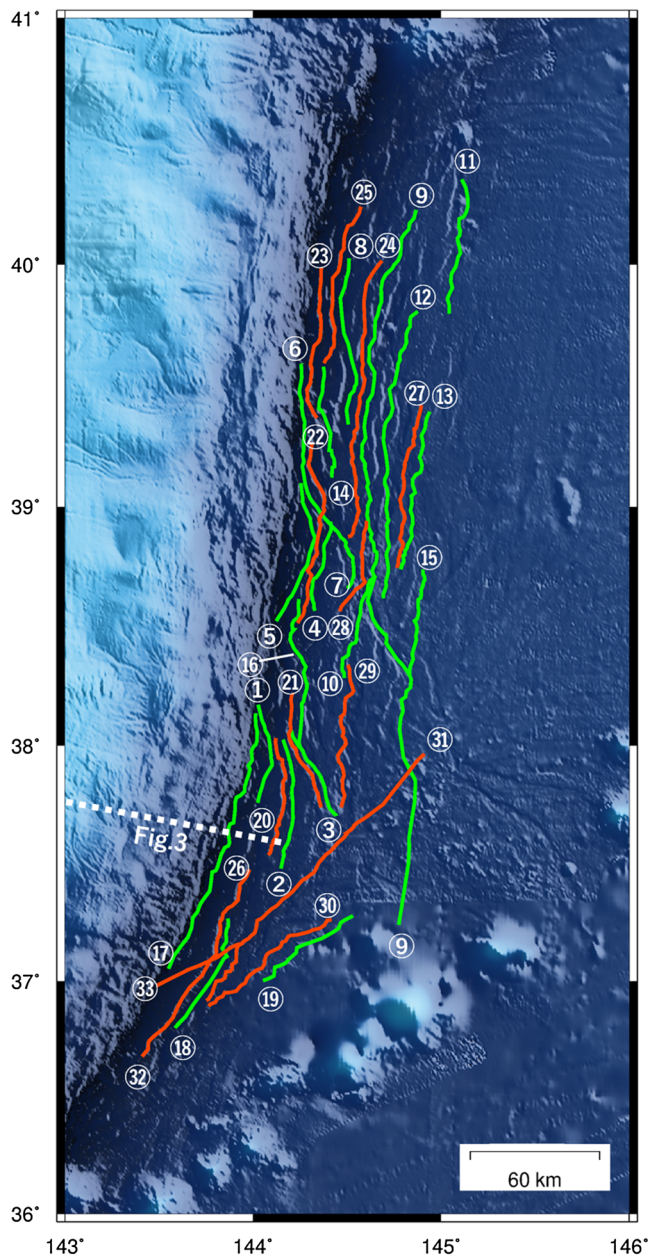


Figure 4. Shaded-relief bathymetric map of the Japan Trench study region (location in Figure 1) showing modeled outer-rise normal fault traces. Green and red lines indicate faults dipping landward (west) and seaward (east), respectively. Basic faults are identified by the encircled numbers. Dotted line is the seismic profile shown in Figure 3.

likely to be moderate at greater depths, ranging from 45° to 60°; and (4) the seismogenic zone for outer-rise earthquakes is approximately 40 km thick. We mapped the seafloor traces of outer-rise faults using the survey data and the criteria proposed by Matsuda (1990). To avoid underestimating the maximum fault surface that could slip at once, discontinuous fault segments with the same dip and strike separated by less than 5 km were considered a single fault. The result was a proposed set of 33 seafloor traces of faults capable of causing significant outer-rise earthquakes in the Japan Trench (Figure 4).

The 33 seafloor traces were extended below the seafloor into rectangular fault planes, referred to here as “basic faults,” for tsunami calculations. Most aspects of the fault models were the same as those adopted for the 2010 Bonin earthquake and tsunami. As with the 2010 Bonin earthquake model, the upper edge of the basic faults was placed at 0.1 km below the seafloor. Dip angles of the basic fault planes were set at 60°, the average value revealed by the seismic surveys (Obana et al., 2012, 2018, 2019). The rake angle was set at 270° under the assumption of pure normal faulting. The width of the basic faults was the same as the fault length ($L = W$) unless the lower edge of the basic fault was deeper than the base of the seismogenic zone (40 km), in which case the width was shortened to match the 40 km depth. The slip amount on the basic fault was determined by the fault area ($L \times W$) and the earthquake magnitude from the scaling law (Álvarez-Gómez et al., 2012), assuming a rigidity of 5×10^{10} N/m². The fault parameters of the 33 basic faults are listed in Table 1.

3.2. Tsunami Calculations of Basic Faults

The same procedure described in section 2 was used for the tsunami calculations of the basic faults. The analytical solution of Okada (1985) was used to calculate displacements at the seafloor, which were then converted to initial sea surface displacements, including the effects of horizontal movements (Tanioka & Satake, 1996b) and the filter based on the linear potential theory (Kajiura, 1963; Saito, 2013, 2019). Propagation of tsunamis from the initial sea surface displacements were calculated from Equations 1–3 using JAGURS tsunami software (Baba et al., 2015, 2017). The bathymetric data were compiled from Japan Coast Guard, GEBCO, and GSI datasets in a model region (30–46°N and 138–150°E) enclosing most of northern Japan (Figure 5). The interval of the computational grid points was 18 arc sec. A nesting algorithm was not applied in the calculations. The time step was 0.4 s and the rise time was 15 s. Tsunami waveforms were calculated for the existing stations, which include ocean-bottom pressure gauges of S-net and DART, GPS buoys, and coastal tide gauges (Figure 5).

The basic fault designated ID 9 ($L = 332$ km, $M_w = 8.7$, Figure 6a and Table 1) produced the largest tsunami (27.0 m) among the 33 basic fault

models. Figure 7 shows the calculated tsunami waveforms from the event on fault ID 9 at three offshore stations and a coastal tide gauge. The distribution of maximum tsunami heights for basic fault ID 9 is shown in Figure 8. Results for the other faults are shown in the supporting information (Figure S1).

3.3. Sensitivity Analysis Using 12 Derived Models

For simplicity, the dip and the rake angles were set at 60° and 270°, respectively, in the basic faults (e.g., Figure 6a). However, actual outer-rise earthquakes would vary from these fixed values. To understand how differences in the fault parameters would affect the accuracy of the tsunami predictions, we

Table 1
Fault Parameters of the Basic Fault Models

ID	Lat. (°) ^a	Lon. (°) ^a	Depth (km)	L (km)	W (km)	Dip (°)	Strike (°)	Rake (°)	Slip (m)	M _w
1	38.1708	144.0276	0.1	46	46	60	180	270	0.4	7.0
2	38.0249	144.1599	0.1	61	46	60	181	270	0.7	7.3
3	38.0646	144.2033	0.1	45	45	60	152	270	0.4	7.0
4	38.9365	144.4128	0.1	42	42	60	190	270	0.4	7.0
5	39.0975	144.2551	0.1	65	46	60	190	270	0.8	7.3
6	39.5916	144.2561	0.1	114	46	60	177	270	2.2	7.8
7	39.5916	144.2561	0.1	106	46	60	168	270	1.9	7.7
8	40.0254	144.5111	0.1	76	46	60	180	270	1.1	7.5
9	40.2224	144.8678	0.1	332	46	60	181	270	15.8	8.7
10	40.2224	144.8678	0.1	218	46	60	189	270	7.3	8.3
11	40.3472	145.1102	0.1	61	46	60	185	270	0.7	7.3
12	39.8068	144.8759	0.1	133	46	60	187	270	2.9	7.9
13	39.3941	144.9400	0.1	74	46	60	190	270	1.0	7.4
14	39.5788	144.3744	0.1	51	46	60	176	270	0.5	7.3
15	38.7381	144.9041	0.1	167	46	60	184	270	4.5	8.1
16	38.6148	144.2442	0.1	103	46	60	170	270	1.8	7.7
17	38.1362	144.0142	0.1	127	46	60	199	270	2.7	7.9
18	37.2671	143.8665	0.1	58	46	60	206	270	0.6	7.2
19	37.2784	144.5308	0.1	52	46	60	234	270	0.5	7.1
20	38.0318	144.1224	0.1	55	46	60	4	270	0.6	7.2
21	38.2164	144.2062	0.1	55	46	60	346	270	0.6	7.2
22	39.2673	144.3149	0.1	84	46	60	5	270	1.3	7.5
23	39.9867	144.3634	0.1	69	46	60	2	270	0.9	7.4
24	40.0149	144.6868	0.1	128	46	60	7	270	2.7	7.9
25	40.2359	144.5756	0.1	73	46	60	13	270	1.0	7.4
26	37.4764	143.9826	0.1	102	46	60	30	270	1.8	7.7
27	39.4220	144.8967	0.1	76	46	60	9	270	1.1	7.4
28	38.9404	144.6059	0.1	44	43	60	17	270	0.4	7.0
29	38.3397	144.5048	0.1	67	46	60	3	270	0.8	7.3
30	37.2620	144.4183	0.1	71	46	60	55	270	0.9	7.4
31	37.9659	144.9115	0.1	155	46	60	41	270	3.9	8.0
32	37.9652	144.9127	0.1	166	46	60	49	270	4.4	8.1
33	37.9659	144.9124	0.1	195	46	60	42	270	6.0	8.2

^aLatitude and longitude mark the north end of the seafloor trace.

conducted a sensitivity analysis by changing the values of selected parameters to derive 12 models from each basic fault model.

Although the dip angle of the faults was set at 60°, it varies in a range from 45° to 75°. For derived Model 1, the dip angle was set at 45° (Figure 6b), and for derived Model 2 it was set at 75° (Figure 6c), and all other parameters were kept unchanged.

The results of seismic imaging showed that the outer-rise faults were dipping steeply at about 75° at shallow depths, a well-constrained result given the high quality of the active-source surveys. However, focal mechanisms from natural earthquakes indicated dip angles at intermediate depths that were less steep, such as 45° and 60°. Together, these results can be interpreted as curved or listric faults, with steep dips near the surface that level off with depth. Therefore, in derived Model 3 (the compound fault model), the fault consisted of an upper half with a 75° dip and a lower half with a 45° dip (Figure 6d).

Because the strike angle was well constrained by the seafloor topography and the distribution of microseismicity, we did not conduct a sensitivity analysis for variations in strike. However, errors would arise from approximating complex sets of unconnected fault segments as a single rectangular fault. Therefore, in derived Model 4 (the subfaults model), we calculated tsunamis from events on a set of small subfaults approximately 40–50 km long in place of the single fault (Figure 6e). During tsunami generations, we might have to consider rupture propagation in the subfaults models for events greater than M8.0. Here, however, we applied simultaneous ruptures on the subfaults because our focus was on the geometric effects of the set of subfaults on prediction of outer-rise tsunamis.

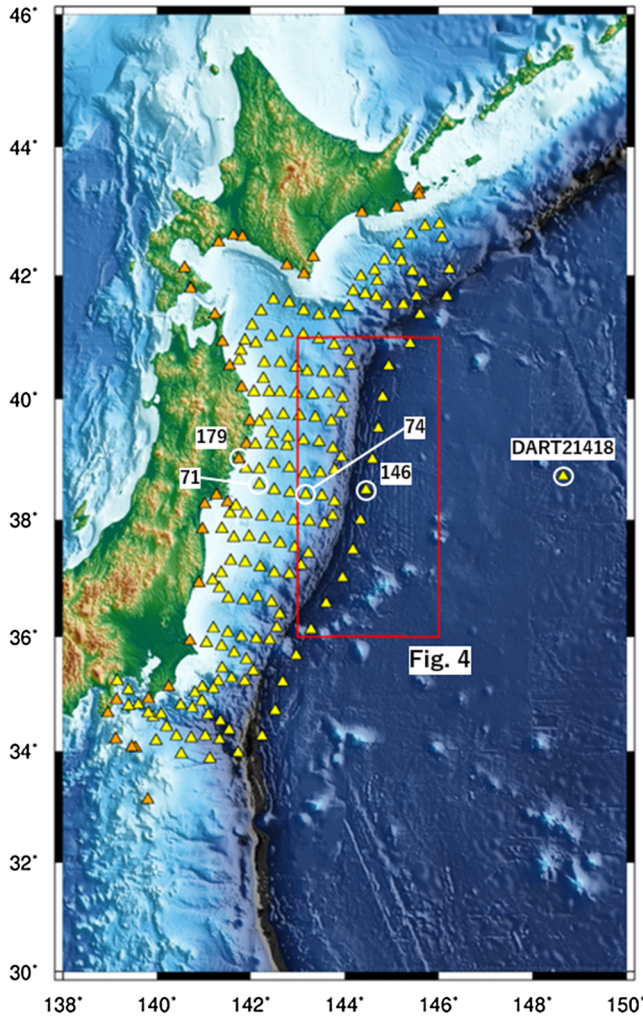


Figure 5. Map of the tsunami simulation region showing the distribution of tsunami stations in northern Japan. Orange triangles are coastal tide gauges and yellow triangles are ocean-bottom pressure gauges. Numbered stations are shown in Figure 7 and discussed in the text. The red box indicates the tsunami source region shown in Figure 4.

Tsunami early warnings rely on rapid solutions of focal mechanisms obtained by seismic wave analysis, but these solutions are prone to errors in their estimated fault parameters. Therefore, we also investigated variations in rake angles with derived Models 5 and 6, which had rake angles of 245° and 285°, respectively.

We calculated earthquake magnitudes for the basic faults with the scaling law of Álvarez-Gómez et al. (2012), which is based on the fault length by the relation $M = 3.89 + 1.89 \log_{10}L$. Álvarez-Gómez et al. (2012) presented an alternative scaling relationship based on source area A ($M = 3.06 + 1.28 \log_{10}A$), obtained by a regression to the same dataset as the original law. Another scaling law was proposed by Blaser et al. (2010) based on terrestrial normal faulting earthquakes ($\log_{10}L = -1.91 + 0.52 M$, $\log_{10}W = -1.20 + 0.36 M$). Derived Model 7 therefore used alternative scaling law of Álvarez-Gómez et al. (2012), or scaling law 2. Derived Model 8 used the scaling law of Blaser et al. (2010), or scaling law 3, constraining the fault width to match the thickness of the seismogenic zone. In these scaling laws, the geometry of faults (length or source area) determines the magnitude of a modeled earthquake, which means that the earthquake magnitude differs according to the applied scaling laws.

In derived Model 9, we changed the governing equations of tsunami propagation from the nondispersive Equations 1 and 2 to the dispersive Equations 4 and 5 because including the dispersion terms had improved the accuracy of our prediction for the 2010 Bonin tsunami (Figure 2b). We discuss this decision in more detail below.

Figure 9 shows the initial sea surface displacement from an earthquake on basic fault ID 9. The steep fault dip resulted in sea surface displacements with short-wavelength components of about 35 km. The phase velocity of linear gravity water waves (LGW), such as tsunamis, is expressed by (Dean & Dalrymple, 1991; Saito, 2019)

$$C_{LGW} = \sqrt{\frac{g\lambda}{2\pi} \tanh \frac{2\pi H}{\lambda}}, \quad (6)$$

where λ is the wavelength and H is the water depth. On the other hand, in the linear longwave approximation (LLW) commonly used in tsunami calculations (Equations 1–3), the phase velocity for the linear case is

$$C_{LLW} = \sqrt{gH}. \quad (7)$$

The difference between C_{LGW} and C_{LLW} is negligible at long wavelengths but large at short wavelengths. For example, in the case shown in Figure 9 ($d = \sim 6$ km, $\lambda = \sim 35$ km), C_{LGW} is ~ 208 m/s and C_{LLW} is ~ 242 m/s. Thus, the LLW must be rejected. On the other hand, the phase velocity from the dispersive model (LDW) such as Equations 4 and 5 (Saito, 2019)

$$C_{LDW} = \sqrt{gH \left(\frac{1}{1 + \frac{1}{3} \left(\frac{2\pi H}{\lambda} \right)^2} \right)}, \quad (8)$$

is $C_{LDW} = \sim 206$ m/s. Accordingly, it is necessary to consider dispersion effects in calculations of tsunamis caused by outer-rise earthquakes. However, the most immediate need from the perspective of disaster response is not a highly accurate tsunami waveform, but a reliable estimate of the maximum tsunami height.

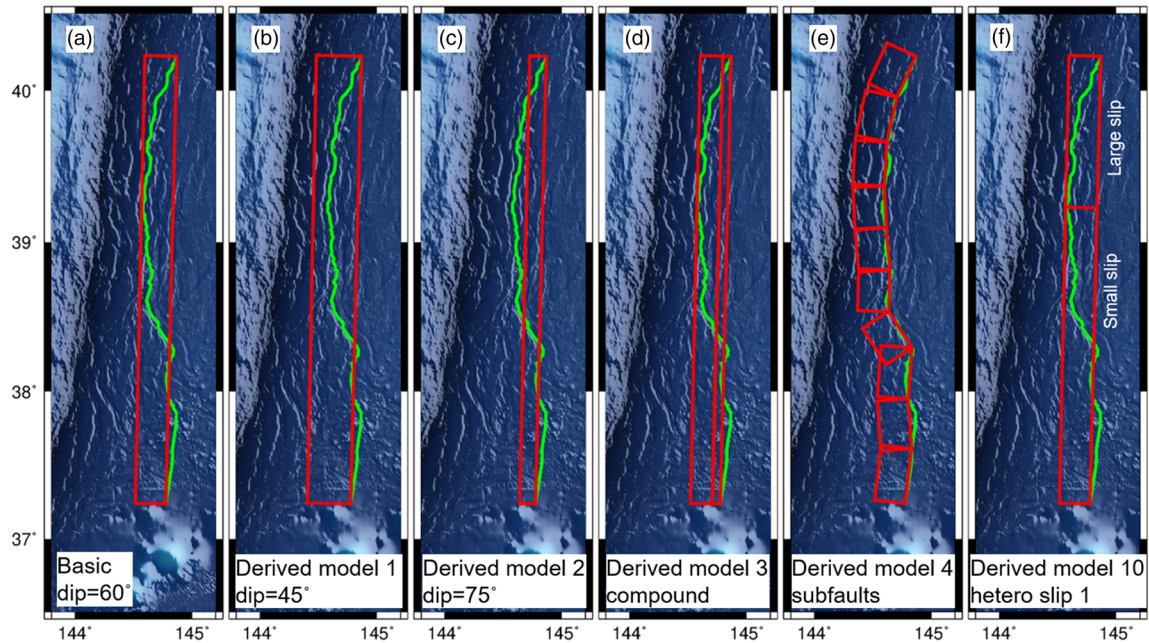


Figure 6. (a–f) Maps showing the seafloor trace of outer-rise fault ID 9 (green) and surface projections of six tested fault models (red). Derived models are described in the text. Each of the 33 faults had its own set of models.

Because actual slip distributions on earthquake fault planes are heterogeneous in space, the homogeneous slip model adopted here for the basic faults may fall short in terms of accurate tsunami predictions. Some recent studies (e.g., Graves & Pitarka, 2010; LeVeque et al., 2016; Mai & Beroza, 2002) have proposed methods to automatically generate heterogeneous slip models for uncertainty studies or probabilistic tsunami hazard assessments. However, there is still room for discussions of how to make spatially

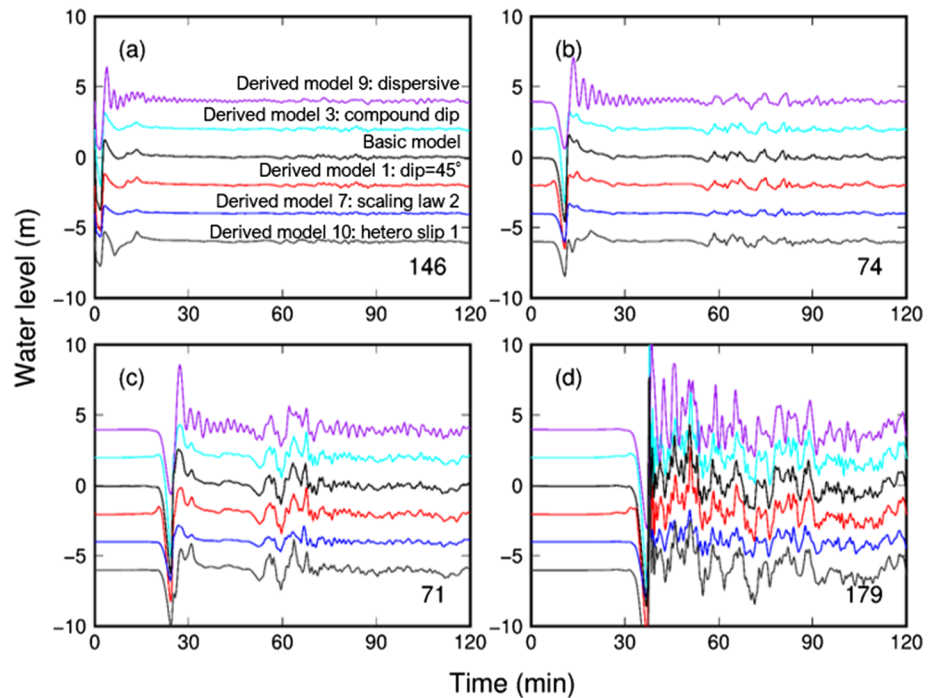


Figure 7. Calculated tsunami waveforms from the maximum earthquake on fault ID 09 at Stations (a) 146, (b) 74, (c) 71, and (d) 179 (locations in Figure 5). Curves are offset vertically for visibility. The six calculation models for the waveforms are labeled in (a) and described in the text.

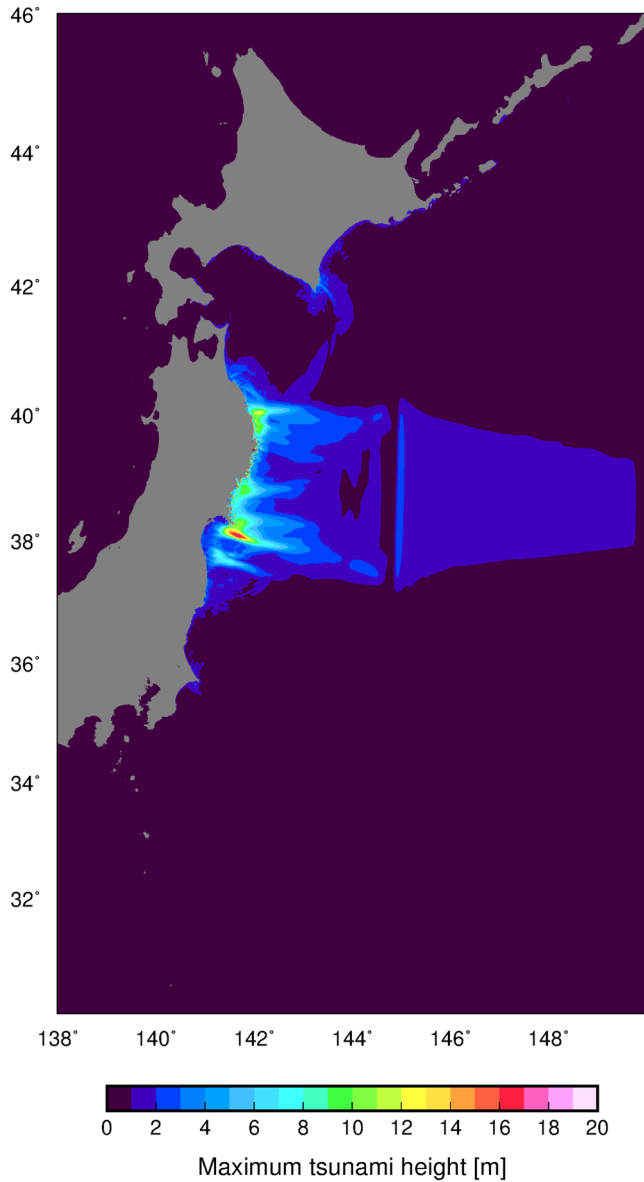


Figure 8. Simulated distribution of maximum tsunami heights from the basic model of fault ID 9.

of K_i and κ_i calculated using all data related to the derived model i (thus, data for all 33 basic models are used to calculate one value of K_i). Tables S1–S4 in the supporting information present the values of K_i and κ_i calculated for each basic model.

According to the results, the most influential factor in the prediction of the maximum tsunami height was the choice of scaling law. The maximum tsunami height calculated by scaling law 2 was as much as 2.5 times greater compared to the basic model (Tables S1 and S2), and scaling law 3 produced tsunamis about 30% smaller on average than the basic model (Figure 10). The heterogeneous slip models increased the maximum tsunami height by 10–15% on average over the basic model. Consideration of dispersion increased the maximum tsunami height by about 10% at the offshore stations and about 5% at the coastal tide stations. Changes in dip angle caused both increases and decreases in tsunami height, depending on the case, but the average difference was less than 5% except for the derived Model 2 (75° dip), in which the tsunami height was systematically reduced by about 10% on average at the coastal stations. The compound model, the subfaults model, and the different rake angle models changed tsunami heights by no more than about 3%.

heterogeneous slip models for the outer-rise earthquakes, and detailed studies of this problem are necessary. In an effort to investigate the effects of heterogeneity of slip on the outer-rise faults within the scope of our study, we constructed derived Models 10–12 on the basis of the following simple method. Each basic fault was divided into three parts along the strike direction. One of the three parts was designated as the large slip area and was assigned twice the slip of the basic fault while the other two parts were assigned half the slip so that the total seismic moment did not change. In derived Models 10–12, the northern, middle, and southern segments, respectively, was defined as the large slip area (Figure 6f).

3.4. Results of Sensitivity Analysis

Figure 7 shows the tsunami waveforms from fault ID 9 along with those from derived Models 1, 3, 7, 9, and 10 vertically shifted for easy comparison. Although the effects of dispersion and heterogeneous slip are plain to see, the differences in maximum tsunami height are difficult to understand from this figure. Therefore, to quantify the differences, we introduced the correlation factors K and κ of Aida (1978):

$$\log K_i = \frac{1}{m} \sum_{j=1}^m \log \frac{\eta_{i,j}^{\max}}{\eta_{0,j}^{\max}}, \quad (9)$$

$$\log \kappa_i = \sqrt{\frac{1}{m} \left\{ \sum_{j=1}^m \left(\log \frac{\eta_{i,j}^{\max}}{\eta_{0,j}^{\max}} \right)^2 - m (\log K_i)^2 \right\}} \quad (10)$$

where $\eta_{i,j}^{\max}$ is the maximum tsunami height at station j obtained by derived model i , $\eta_{0,j}^{\max}$ is the maximum tsunami height at station j obtained by the basic fault model, and m is the number of stations. The station data consisted of the maximum tsunami height at the sites of the coastal tide gauges, the GPS buoys, the pressure gauges of S-net, and the DART stations (Figure 5). K_i is the geometric average of the ratio between the maximum tsunami heights of derived model i and those of the basic model; values above 1 signify that the maximum tsunami heights from the derived model are larger on average than those of the basic model. κ_i is the geometric standard deviation indicating the variance of $\eta_{i,j}^{\max}/\eta_{0,j}^{\max}$; values close to 1 are better. We calculated K_i and κ_i values separately for the offshore stations and the coastal stations. Figure 10 shows the values

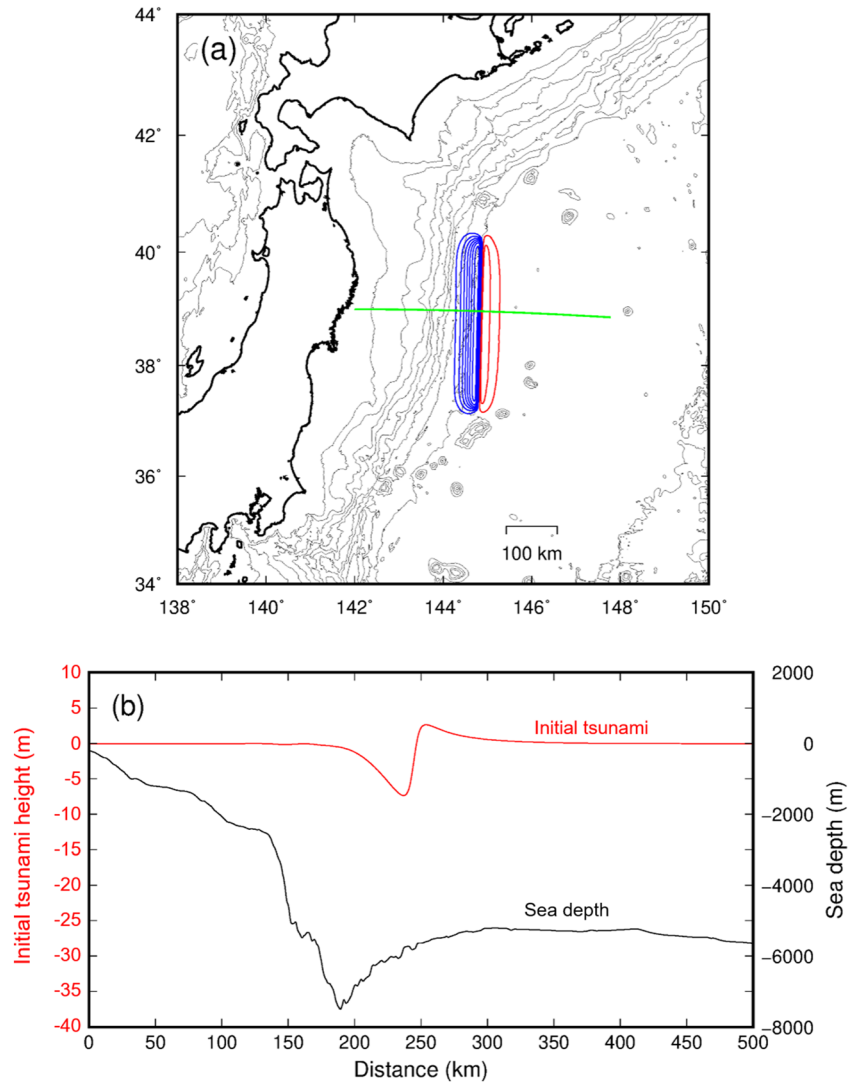


Figure 9. (a) Initial sea surface displacements due to faulting by the basic model of fault ID 9. Red and blue contours are uplift and subsidence, respectively, with contour interval of 1 m. Thin gray lines are bathymetry with contour interval of 1,000 m. (b) Initial sea surface displacement (red) and bathymetry (black) along the green line in (a).

4. Discussion

4.1. Importance of Scaling Law for Tsunami Predictions

The selection of an appropriate earthquake scaling law is important for predicting tsunamis caused by earthquakes. We investigated three of them in this study. The first and second laws are based on data from past outer-rise earthquakes (Álvarez-Gómez et al., 2012), and the third law is based on data from normal faulting earthquakes, including inland events. Because the third scaling law reduced the tsunami height by 30% with respect to the basic model (Figure 10), the importance of using scaling laws tailored for outer-rise earthquakes is clear.

The first and second laws were both proposed by Álvarez-Gómez et al. (2012), who approximated the magnitudes of the 12 outer-rise earthquakes around the world by regression lines for the fault length and the fault area, respectively. At $M8.4$, the 1933 Showa Sanriku earthquake was the largest of these events. The determination coefficients R^2 were 0.78 for the first scaling law and 0.66 for the second indicating a slightly better fit to the data with the first law. For that reason, we applied the first law in the basic model of this study. Although the two scaling laws differed only in using fault length versus fault

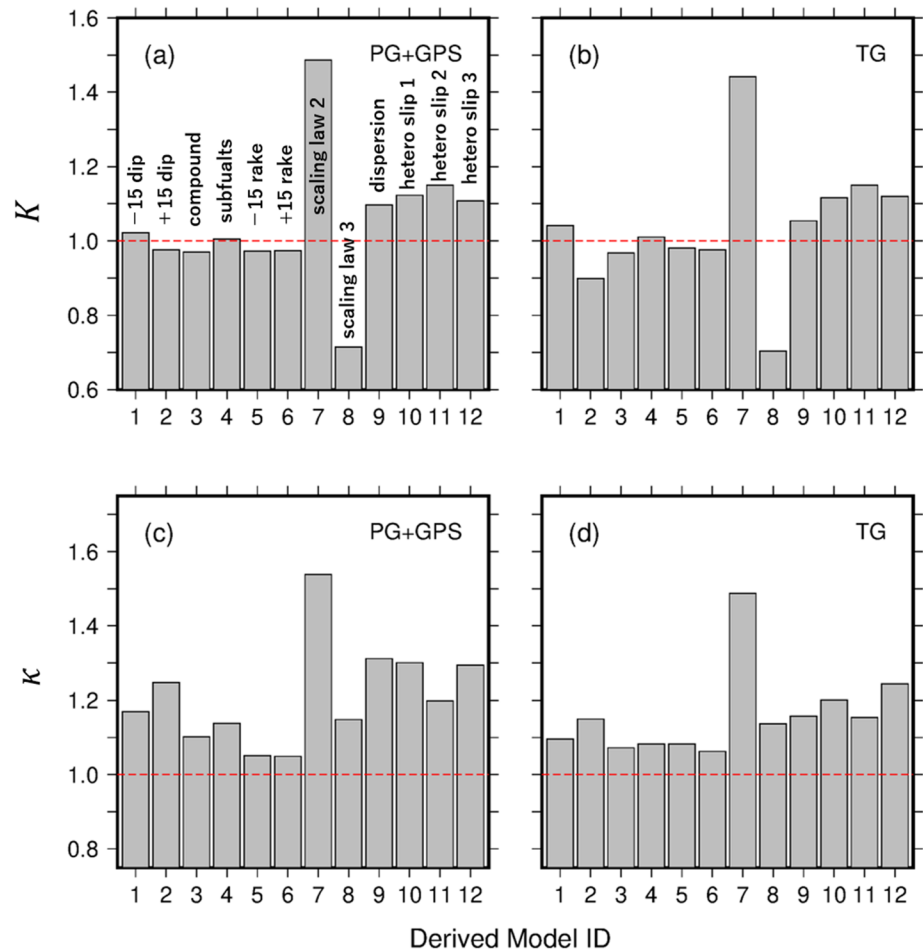


Figure 10. Values of K and κ (Aida, 1978) for the 12 derived models, calculated by taking into account all 33 basic models. See text for model descriptions: (a) K for offshore stations of pressure gauges and GPS buoys (PG + GPS), (b) K for coastal tide gauges (TG), (c) κ for offshore stations, and (d) κ for coastal tide gauges. K and κ calculated for all basic models are listed in Tables S1 and S2 in the supporting information.

area in the regression analysis, the difference in the predicted tsunamis was very large as indicated by the K value of 1.5 (Figure 10). It is clear, then, that the earthquake scaling law used in tsunami predictions for outer-rise earthquakes should be chosen with great care. Álvarez-Gómez et al. (2012) compiled data from only 12 outer-rise earthquakes to derive their scaling laws, and need for obtaining more data is obvious.

4.2. Amplification of Tsunami Due to Heterogeneous Slips

As previous studies have found (Crempien et al., 2020; Li et al., 2016; Melgar et al., 2019), this study shows that the heterogeneous slips have a big impact on predicted tsunamis. The concentration of slip in our derived Models 10–12 caused spatial heterogeneity in the initial tsunami source, resulting in large variations of tsunami height along the coast. Because the heterogeneous slip models had the same seismic moment as the basic fault model, the slip amounts in the large slip areas were larger than that of the basic fault and the slip amounts in the other areas were smaller. We thought that the tsunami at the coastline facing the large-slip area would certainly be higher than the basic fault tsunami and smaller than it elsewhere. Therefore, the value of K , which is an average of multiple observation points (Figure 5), was expected to be near 1, while κ , the indicator of variation, would increase. However, the heterogeneous slip models yielded K estimates of 1.10–1.15. We were surprised that the heterogeneous slip models generated tsunamis 10–15% higher on average than the basic fault models did. The effects

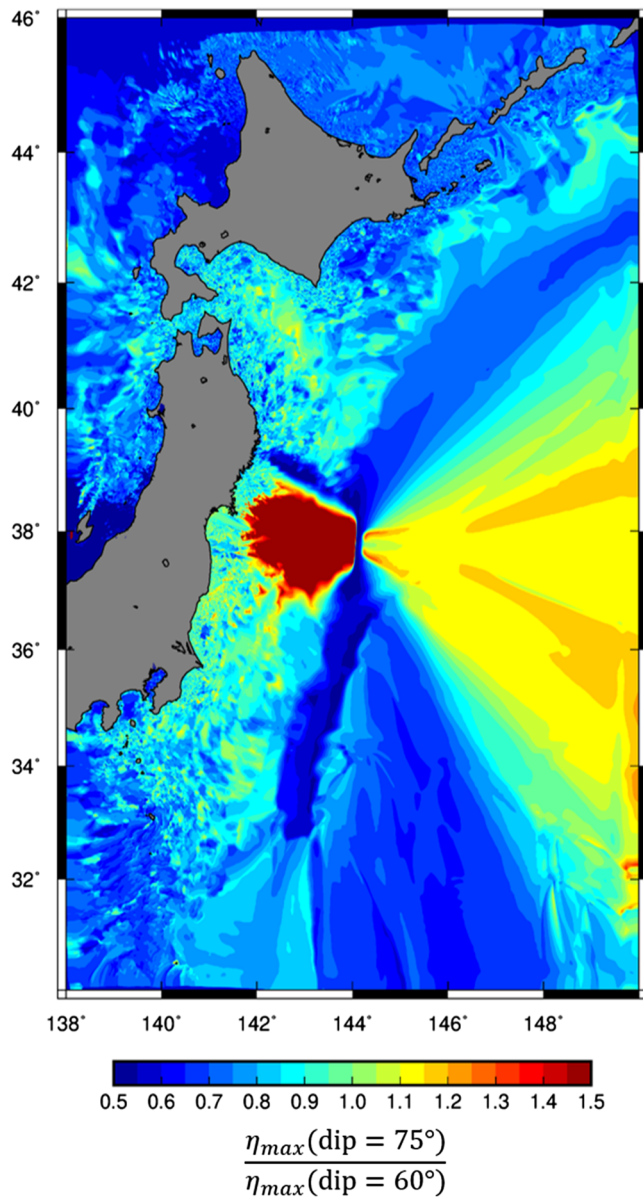


Figure 11. Ratio of the maximum tsunami heights from the steep-dipping (75°) model and the basic (60° dip) model of fault ID20. This ratio is equivalent to K of Aida (1978). Note that $K < 1$ in much of the region.

lations using the linear longwave equations that remove the advection and friction terms from Equations 1–3, the average value of K for all models was 0.920, only slightly changed from the average value of K (0.898) of the original estimation using the nonlinear longwave equations. We conclude that the advection and friction terms were not primarily responsible for reducing the maximum tsunami height at the coast from high-angle faults. We speculate that the steeper fault produced smaller tsunamis as a result of the complexity of tsunami propagation near the coast. Tsunamis can be transformed by the effects of shoaling, refractions, reflections, and resonances in bays. Our simulated tsunami waveforms showed that whereas the first wave was always the highest one at the offshore stations, this was not true for the coastal tide gauges. In sum, the relationship between fault dip angle and maximum tsunami height along the coast is determined not only by the initial water level at the tsunami source but also by the nearshore bathymetry; thus, greater maximum seafloor displacements at the tsunami source do not always mean higher tsunami waves at the coast.

of heterogeneous slips also are subject to the complicating effects of bathymetry and travel distance between the tsunami source and the coast. Detailed investigations are necessary before the effects of heterogeneous slips in outer-rise earthquakes can be confidently applied to tsunami predictions.

Fault parameters obtained by rapid analysis of seismic waves are used in almost every early tsunami warning system in operation. They provide estimates of the fault geometry, the direction of slip, and the event magnitude but provide no information about the spatial slip distribution on the fault plane. Our study shows that heterogeneous slips on the fault appear to have large effects in tsunami predictions. It would be desirable to determine slip distributions using seismic waves in real time for next-generation early tsunami warning. Lacking that, predictions should incorporate real-time tsunami data from offshore stations such as ocean-bottom pressure gauges and GPS buoys. Direct utilization of offshore tsunami data in real time for operational early tsunami warning may be enhanced by using several innovative tsunami prediction techniques recently proposed by such as those of Igarashi et al. (2016), Maeda et al. (2015), and Wang et al. (2017).

4.3. Influence of Dip Angle

As the dip of a fault increases, the maximum seafloor displacement due to the fault slip increases, and the wavelength of the deformation shortens. Thus, the steeper the fault dip, the larger the initial displacement (initial tsunami) at the sea surface. One might thus expect that larger tsunamis would be observed at stations as fault dip increase (thus, $K > 1.0$). However, Table S1 shows that as an average for all offshore stations, tsunamis caused by faults with 75° dips were not always larger, and tsunamis caused by faults with 45° dips were not always smaller than those caused by the basic faults with 60° dips. The explanation lies in the directivity of tsunami propagation, as shown in Figure 11 for fault model ID 20. In that simulation, the value of K , that is, the ratio of maximum tsunami height caused by the same model with dips of 75° and 60°, is greater than 1 in a limited area in the direction perpendicular to the fault strike, and in the remaining large areas it is smaller than 1. Because the value of K listed in Table S1 is the average of the height ratio at all stations, it does not reflect the maximum height in the initial tsunami from a given event. This interpretation is reasonable given the fact that the value of K for the smaller earthquakes tends to fall below 1.0.

On the other hand, at coastal stations the average values of K of a fault with 75° dip were below 1.0 for all fault models (Table S2). When we ran calculations using the linear longwave equations that remove the advection and friction terms from Equations 1–3, the average value of K for all models was 0.920, only slightly changed from the average value of K (0.898) of the original estimation using the nonlinear longwave equations. We conclude that the advection and friction terms were not primarily responsible for reducing the maximum tsunami height at the coast from high-angle faults. We speculate that the steeper fault produced smaller tsunamis as a result of the complexity of tsunami propagation near the coast. Tsunamis can be transformed by the effects of shoaling, refractions, reflections, and resonances in bays. Our simulated tsunami waveforms showed that whereas the first wave was always the highest one at the offshore stations, this was not true for the coastal tide gauges. In sum, the relationship between fault dip angle and maximum tsunami height along the coast is determined not only by the initial water level at the tsunami source but also by the nearshore bathymetry; thus, greater maximum seafloor displacements at the tsunami source do not always mean higher tsunami waves at the coast.

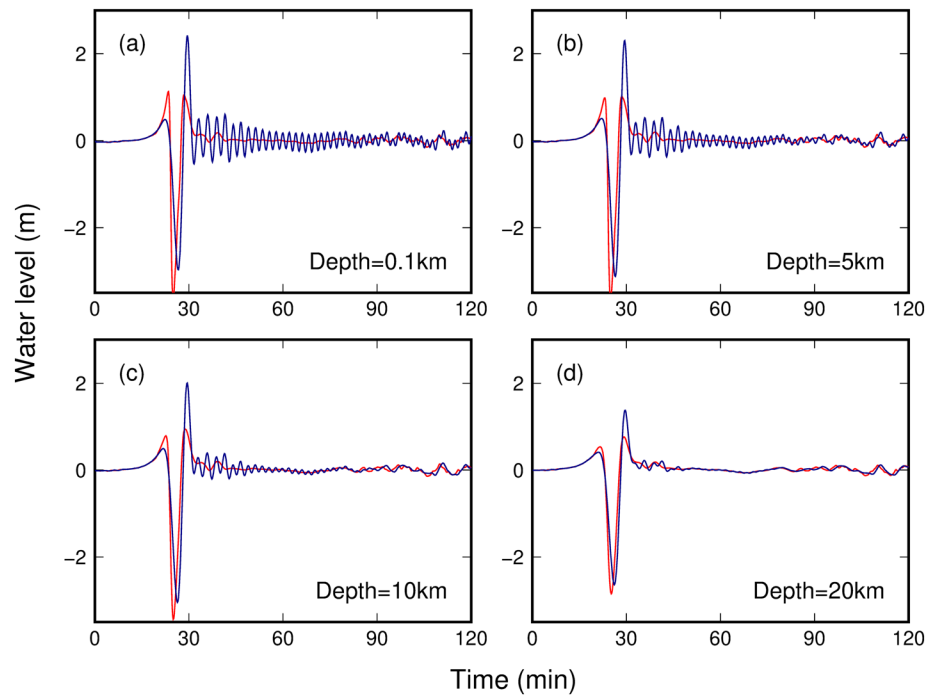


Figure 12. Calculated tsunami waveforms from fault ID 9 at stations DART21418 (location in Figure 5) with differing upper depths of the fault: (a) 0.1, (b) 5, (c) 10, and (d) 20 km. Red and blue waveforms were obtained by the nondispersive and dispersive equations, respectively.

4.4. Dispersive Effects

The wavelength of the initial sea surface displacements caused by the outer-rise earthquakes (Figure 9) is too short to fit by the nondispersive Equations 1–3. Tables S1 and S2 show that the inclusion of dispersion increased predicted tsunamis, as measured by K , by about 5% for coastal stations and 10% for offshore stations. Further, the maximum tsunami heights obtained by the dispersive equations were greater than those obtained by the nondispersive (longwave) equations. Dispersion causes tsunami wave trains to spread out, and it usually results in smaller maximum tsunami heights for the case of a pushing-dominant (positive) wave. However, for the case of a pulling-dominant (negative) wave typically caused by outer-rise earthquakes, dispersion produces the opposite effect and increases the maximum tsunami height, as shown in the waveforms of Figures 2b and 12a. This aspect of dispersion was also previously recognized in the case of submarine landslide tsunamis by Baba et al. (2019). Because underestimations of a tsunami are not acceptable for disaster management agencies tasked with safeguarding lives and properties, it is desirable to include this effect when predicting maximum heights of tsunamis caused by outer-rise earthquakes.

Dispersion is indispensable for accurate simulations of tsunamis from outer-rise earthquakes. The difference between tsunami waveforms calculated with dispersive and nondispersive equations is shown for the 2010 Bonin tsunami at DART21413 in Figure 2b. The prediction was more accurate with the use of dispersive equations. Similar results were reported by Zhou et al. (2012) for the tsunami caused by the 2009 Samoa outer-rise earthquake and by Tanioka et al. (2018) for the tsunami caused by the 2016 El Salvador-Nicaragua outer-rise earthquake.

Our simulations placed the upper edge of the basic faults at 0.1 km below the seafloor on the basis of seismic surveys. Shallow faulting causes steep seafloor displacements that result in tsunami waves with short wavelengths. These waves are susceptible to being deformed by dispersion effects. However, dispersion is also influential for deeper faulting, as shown by our simulations in which the top of the fault zone was increased to depths as great as 20 km (Figure 12). It is important to better understand outer-rise earthquakes in order to reduce damages due to shaking and tsunamis, but the mechanisms of outer-rise earthquakes are not well

understood. This study shows that dispersive equations can resolve fault motions at moderate as well as very shallow depths. The use of dispersive equations may help reveal the detailed fault motions of outer-rise earthquakes as well as improve predictions of the tsunamis they cause.

5. Conclusion

In this study we investigated a method to perform numerical tsunami simulations for outer-rise earthquakes, using estimated seafloor displacements to estimate the initial sea surface displacements. Tsunami propagations were then calculated by using either nondispersive equations or dispersive equations in JAGURS software. We validated our method using tsunami observations from the 2010 Bonin outer-rise earthquake and found that dispersive equations yielded the best agreement with the observed waveforms of the 2010 Bonin tsunami at a seafloor observatory.

We applied the validated method to the Japan Trench, where we simulated tsunamis caused by the largest possible earthquakes from 33 faults mapped in an intensively surveyed area of the outer rise, seaward of the trench, extending from 36.5°N to 40.5°N. The largest tsunami we predicted, from an earthquake on fault ID 9 ($L = 332$ km, $M_w = 8.7$), reached a height of 27.0 m at the coast of northeast Japan. We performed sensitivity tests to evaluate the effects of uncertainties in the assumed fault parameters and the modeling procedures and reached the following conclusions:

1. The largest variation in predicted maximum tsunami heights arose from the selection of the earthquake scaling law. Even similar scaling laws constructed using the same dataset predicted widely dissimilar tsunami heights. Therefore, it is necessary to carefully select the earthquake scaling law when predicting tsunamis from outer-rise earthquakes.
2. Heterogeneous slips have a large impact on tsunami predictions for outer-rise earthquakes. The maximum tsunami heights from the heterogeneous slip models increased by 10–15% on average over those from the basic models. Because the degree of heterogeneity in our models was small in this study, much work remains to be done before reaching quantitative conclusions on the effects of slip heterogeneity on tsunami predictions.
3. The strike angles of the 33 outer-rise faults were well constrained by the seafloor topography and seismicity distribution. Seismic surveys indicated that fault dips ranged from 45° to 75°. Variations of $\pm 15^\circ$ in dip angle produced differences as large as 10% in maximum tsunami heights at the coast.
4. Effects of wave dispersion produced differences in predicted tsunami heights comparable to those resulting from $\pm 15^\circ$ changes in dip. Dispersion made tsunami waves higher in pulling-dominant tsunamis caused by the normal faulting events typical of outer-rise earthquakes, unlike the case of pushing-dominant tsunamis caused by thrust faulting events. Increases in maximum tsunami heights due to dispersion were especially notable at the offshore stations. This finding is an important consideration for officials involved in disaster prevention measures, who must avoid underestimations in tsunami predictions.

Data Availability Statement

We used tsunami software JAGURS (Baba et al., 2015, 2017) provided in an online repository at <https://doi.org/10.5281/zenodo.3737816> on the Earth Simulator at JAMSTEC. We also used GMT (Wessel et al., 2013) for data handling and plotting.

Acknowledgments

We thank two anonymous reviewers, the Associate Editor, and the Editor, Dr. Rachel Abercrombie, whose constructive comments improved the manuscript. This work was supported by JSPS KAKENHI Grants 15H05718 and 19H02409.

References

- Abe, K. (1978). A dislocation model of the 1933 Sanriku earthquake consistent with the tsunami waves. *Journal of Physics of the Earth*, 26(4), 381–396. <https://doi.org/10.4294/jpe1952.26.381>
- Aida, I. (1978). Reliability of a tsunami source model derived from fault parameters. *Journal of Physics of the Earth*, 26(1), 57–73. <https://doi.org/10.4294/jpe1952.26.57>
- Álvarez-Gómez, J. A., Gutiérrez, O. Q. G., Aniel-Quiroga, Í., & González, M. (2012). Tsunamigenic potential of outer-rise normal faults at the Middle America trench in Central America. *Tectonophysics*, 574–575, 133–143. <https://doi.org/10.1016/j.tecto.2012.08.014>
- Ammon, C. J., Kanamori, H., & Lay, T. (2008). A great earthquake doublet and seismic stress transfer cycle in the central Kuril islands. *Nature*, 451(7178), 561–565. <https://doi.org/10.1038/nature06521>
- Baba, T., Allgeyer, S., Hossen, J., Cummins, P. R., Tsushima, H., Imai, K., et al. (2017). Accurate numerical simulation of the far-field tsunami caused by the 2011 Tohoku earthquake, including the effects of Boussinesq dispersion, seawater density stratification, elastic loading, and gravitational potential change. *Ocean Modelling*, 111, 46–54. <https://doi.org/10.1016/j.ocemod.2017.01.002>

- Baba, T., Cummins, P. R., Thio, H. K., & Tsushima, H. (2009). Validation and joint inversion of teleseismic waveforms for earthquake source models using deep ocean bottom pressure records: A case study of the 2006 Kuril megathrust earthquake. *Pure and Applied Geophysics*, *166*(1–2), 55–76. <https://doi.org/10.1007/s00024-008-0438-1>
- Baba, T., Gon, Y., Imai, K., Yamashita, K., Matsuno, T., Hayashi, M., & Ichihara, H. (2019). Modeling of a dispersive tsunami caused by a submarine landslide based on detailed bathymetry of the continental slope in the Nankai trough, southwest Japan. *Tectonophysics*, *768*, 228182. <https://doi.org/10.1016/j.tecto.2019.228182>
- Baba, T., Takahashi, N., & Kaneda, Y. (2014). Near-field tsunami amplification factors in the Kii Peninsula, Japan for Dense Ocean Floor Network for Earthquakes and Tsunamis (DONET). *Marine Geophysical Researches*, *35*(3), 319–325. <https://doi.org/10.1007/s11001-013-9189-1>
- Baba, T., Takahashi, N., Kaneda, Y., Ando, K., Matsuoka, D., & Kato, T. (2015). Parallel implementation of dispersive tsunami wave modeling with a nesting algorithm for the 2011 Tohoku tsunami. *Pure and Applied Geophysics*, *172*(12), 3455–3472. <https://doi.org/10.1007/s00024-015-1049-2>
- Blaser, L., Krüger, F., Ohrnberger, M., & Scherbaum, F. (2010). Scaling relations of earthquake source parameter estimates with special focus on subduction environment. *Bulletin of the Seismological Society of America*, *100*(6), 2914–2926. <https://doi.org/10.1785/0120100111>
- Boston, B. B., Moore, G. F., Nakamura, Y., & Kodaira, S. (2014). Outer-rise normal fault development and influence on near-trench décollement propagation along the Japan Trench, off Tohoku. *Earth, Planets and Space*, *66*(1), 135. <https://doi.org/10.1186/1880-5981-66-135>
- Chiba, T., Kaneta, S., & Suzuki, Y. (2008). Red relief image map: New visualization method for three dimensional data. *The International Archives of the Photogrammetry, Remote Sensing and Spatial Information Sciences*, *37*, 1071–1076.
- Crempien, J. G. F., Urrutia, A., Benavente, R., & Cienfuegos, R. (2020). Effects of earthquake spatial slip correlation on variability of tsunami potential energy and intensities. *Scientific Reports*, *10*(1). <https://doi.org/10.1038/s41598-020-65412-3>
- Dean, R. G., & Dalrymple, R. A. (1991). *Water wave mechanics for engineers and scientist* (Vol. 2). Singapore: World Scientific Publishing Company.
- Fujie, G., Kodaira, S., Nakamura, Y., Morgan, J. P., Dannowski, A., Thorwart, M., et al. (2020). Spatial variations of incoming sediments at the northeastern Japan arc and their implications for megathrust earthquakes. *Geology*, *48*(6), 614–619. <https://doi.org/10.1130/G46757.1>
- Fujie, G., Kodaira, S., Sato, T., & Takahashi, T. (2016). Along-trench variations in the seismic structure of the incoming Pacific plate at the outer rise of the northern Japan trench. *Geophysical Research Letters*, *43*, 666–673. <https://doi.org/10.1002/2015GL067363>
- Fujii, Y., & Satake, K. (2008). Tsunami sources of November 2006 and January 2007 great Kuril earthquakes. *Bulletin of the Seismological Society of America*, *98*(3), 1559–1571. <https://doi.org/10.1785/0120070221>
- Graves, R. W., & Pitarka, A. (2010). Broadband ground-motion simulation using a hybrid approach. *Bulletin of the Seismological Society of America*, *100*(5A), 2095–2123. <https://doi.org/10.1785/0120100057>
- Greenslade, D. J. M., Allen, S. C. R., & Simanjuntak, M. A. (2011). An evaluation of tsunami forecasts from the T2 scenario database. *Pure and Applied Geophysics*, *168*(6–7), 1137–1151. <https://doi.org/10.1007/s00024-010-0229-3>
- Greenslade, D. J. M., Annunziato, A., Babeyko, A. Y., Burbidge, D. R., Ellguth, E., Horspool, N., et al. (2014). An assessment of the diversity in scenario-based tsunami forecasts for the Indian Ocean. *Continental Shelf Research*, *79*, 36–45. <https://doi.org/10.1016/j.csr.2013.06.001>
- Igarashi, Y., Hori, T., Murata, S., Baba, T., & Okada, M. (2016). Maximum tsunami height prediction using pressure gauge data by a Gaussian process at Owase in the Kii Peninsula, Japan. *Marine Geophysical Researches*, *37*(4), 361–370. <https://doi.org/10.1007/s11001-016-9286-z>
- Japan Hydrographic Association (2017). *M7000 digital bathymetric chart (M7023)*. Tokyo: Japan Hydrographic Association. https://www.jha.or.jp/shop/index.php?main_page=index&language=en (last access on July 16, 2020).
- Kajiura, K. (1963). The leading wave of a tsunami. *Bulletin of the Earthquake Research Institute*, *41*, 535–571.
- Kanamori, H. (1971). Seismological evidence for a lithospheric normal faulting—The Sanriku earthquake of 1933. *Physics of the Earth and Planetary Interiors*, *4*(4), 289–300. [https://doi.org/10.1016/0031-9201\(71\)90013-6](https://doi.org/10.1016/0031-9201(71)90013-6)
- Kato, T., Terada, Y., Ito, K., Hattori, R., Abe, T., Miyake, T., et al. (2005). Tsunami due to the 2004 September 5th off the Kii peninsula earthquake, Japan, recorded by a new GPS buoy. *Earth, Planets and Space*, *57*(4), 297–301.
- Kodaira, S., Nakamura, Y., Yamamoto, Y., Obana, K., Fujie, G., No, T., et al. (2017). Depth-varying structural characters in the rupture zone of the 2011 Tohoku-oki earthquake. *Geosphere*, *13*(5), 1408–1424. <https://doi.org/10.1130/GES01489.1>
- Kodaira, S., Ohira, A., Fujie, G., No, T., Nakamura, Y., Kaiho, Y., & Miura, S. (2019). Seismic image of the incoming oceanic crust entering the central part of the Japan Trench: Structural variation caused by petit-spot, bend fault and seamount. *Japan Geoscience Union Meeting, 2019*, SCG60–SCG07.
- Lay, T., Ammon, C. J., Kanamori, H., Rivera, L., Koper, K. D., & Hutko, A. R. (2010). The 2009 Samoa-Tonga great earthquake triggered doublet. *Nature*, *466*(7309), 964–968. <https://doi.org/10.1038/nature09214>
- Lay, T., Kanamori, H., Ammon, C. J., Hutko, A. R., Furlong, K., & Rivera, L. (2009). The 2006–2007 Kuril Islands great earthquake sequence. *Journal of Geophysical Research*, *114*, B11308. <https://doi.org/10.1029/2008JB006280>
- LeVeque, R. J., Waagan, K., González, F. I., Rim, D., & Lin, G. (2016). Generating random earthquake events for probabilistic tsunami hazard assessment. In *Global tsunami science: Past and future* (Vol. I, pp. 3671–3692). Basel, Switzerland: Birkhäuser.
- Li, L., Switzer, A. D., Chan, C.-H., Wang, Y., Weiss, R., & Qiu, Q. (2016). How heterogeneous coseismic slip affects regional probabilistic tsunami hazard assessment: A case study in the South China Sea. *Journal of Geophysical Research: Solid Earth*, *121*, 6250–6272. <https://doi.org/10.1002/2016JB013111>
- Maeda, T., Obara, K., Shinohara, M., Kanazawa, T., & Uehira, K. (2015). Successive estimation of a tsunami wavefield without earthquake source data: A data assimilation approach toward real-time tsunami forecasting. *Geophysical Research Letters*, *42*, 7923–7932. <https://doi.org/10.1002/2015GL065588>
- Mai, P. M., & Beroza, G. C. (2002). A spatial random field model to characterize complexity in earthquake slip. *Journal of Geophysical Research*, *107*(B11), 2308. <https://doi.org/10.1029/2001JB000588>
- Matsuda, T. (1990). Seismic zoning map of Japanese Islands, with maximum magnitude derived from active fault data. *Bulletin of the Earthquake Research Institute*, *65*, 415–422.
- Melgar, D., Williamson, A. L., & Salazar-Monroy, E. F. (2019). Differences between heterogenous and homogenous slip in regional tsunami hazards modelling. *Geophysical Journal International*, *219*, 553–562. <https://doi.org/10.1093/gji/ggz299>
- National Research Institute for Earth Science and Disaster Resilience, NIED S-net (2019). <https://doi.org/10.17598/nied.0007>

- Nayak, S., & Kumar, T. S. (2008a). The first tsunami early warning centre in the Indian Ocean. In *Risk Wise* (pp. 175–177). UK: Tudor Rose Publications.
- Nayak, S., & Kumar, T. S. (2008b). Addressing the risk of the tsunami in the Indian Ocean. *Journal of South Asia Disaster Studies*, *1*, 45–57.
- Necmioğlu, Ö., & Özel, N. M. (2014). An earthquake source sensitivity analysis for tsunami propagation in the Eastern Mediterranean. *Oceanography*, *27*(2), 76–85. <https://doi.org/10.5670/oceanog.2014.42>
- Obana, K., Fujie, G., Takahashi, T., Yamamoto, Y., Nakamura, Y., Kodaira, S., et al. (2012). Normal-faulting earthquakes beneath the outer slope of the Japan Trench after the 2011 Tohoku earthquake: Implications for the stress regime in the incoming Pacific plate. *Geophysical Research Letters*, *39*, L00G24. <https://doi.org/10.1029/2011GL050399>
- Obana, K., Fujie, G., Takahashi, T., Yamamoto, Y., Tonegawa, T., Miura, S., & Kodaira, S. (2019). Seismic velocity structure and its implications for oceanic mantle hydration in the trench–outer rise of the Japan Trench. *Geophysical Journal International*, *217*, 1629–1642. <https://doi.org/10.1093/gji/ggz099>
- Obana, K., Nakamura, Y., Fujie, G., Kodaira, S., Kaiho, Y., Yamamoto, Y., & Miura, S. (2018). Seismicity in the source areas of the 1896 and 1933 Sanriku earthquakes and implications for large near-trench earthquake faults. *Geophysical Journal International*, *212*, 2061–2072. <https://doi.org/10.1093/gji/ggx532>
- Okada, Y. (1985). Surface deformation due to shear and tensile faults in a half-space. *Bulletin of the Seismological Society of America*, *75*, 1435–1154.
- Okal, E. A., Fritz, H. M., Synolakis, C. E., Borrero, J. C., Weiss, R., Lynett, P. J., et al. (2010). Field survey of the Samoa tsunami of 29 September 2009. *Seismological Research Letters*, *81*(4), 577–591. <https://doi.org/10.1785/gssrl.81.4.577>
- Peregrine, H. (1972). Equations for water waves and the approximations behind them. In R. E. Meyer (Ed.), *Waves on beaches and resulting sediment transport* (pp. 95–121). New York: academic press.
- Saito, T. (2013). Dynamic tsunami generation due to sea-bottom deformation: Analytical representation based on liner potential theory. *Earth, Planets and Space*, *65*(12), 1411–1423. <https://doi.org/10.5047/eps.2013.07.004>
- Saito, T. (2019). Tsunami generation and propagation, 265pp. *Springer Geophysics*. https://doi.org/10.1007/978-4-431-56850-6_1
- Tanioka, Y., Ramirez, A. G. C., & Yamanaka, Y. (2018). Simulation of a dispersive tsunami due to the 2016 El Salvador-Nicaragua outer-rise earthquake (*M*_w 6.9). *Pure and Applied Geophysics*, *175*(4), 1363–1370. <https://doi.org/10.1007/s00024-018-1773-5>
- Tanioka, Y., & Satake, K. (1996a). Fault parameters of the 1896 Sanriku tsunami earthquake estimated from tsunami numerical modeling. *Geophysical Research Letters*, *23*(13), 1549–1552. <https://doi.org/10.1029/96GL01479>
- Tanioka, Y., & Satake, K. (1996b). Tsunami generation by horizontal displacement of ocean bottom. *Geophysical Research Letters*, *23*(8), 861–864. <https://doi.org/10.1029/96GL00736>
- Tsushima, H., Hino, R., Fujimoto, H., Tanioka, Y., & Imamura, F. (2009). Near-field tsunami forecasting from cabled ocean bottom pressure data. *Journal of Geophysical Research*, *114*, B06309. <https://doi.org/10.1029/2008JB005988>
- Tsushima, H., Hino, R., Tanioka, Y., Imamura, F., & Fujimoto, H. (2012). Tsunami waveform inversion incorporating permanent seafloor deformation and its application to tsunami forecasting. *Journal of Geophysical Research*, *117*, B03311. <https://doi.org/10.1029/2011JB008877>
- U.S. Geological Survey (2010). *M7.4-Bonin Islands, Japan region, Earthquake hazards program*. USA: U.S. Geological Survey. Retrieved from <https://earthquake.usgs.gov/earthquakes/eventpage/usp000hr97/executive>
- Uchida, N., Kirby, S. H., Umino, N., Hino, R., & Kazakami, T. (2016). The great 1933 Sanriku-oki earthquake: Reappraisal of the mainshock and its aftershocks and implications for its tsunami using regional tsunami and seismic data. *Geophysical Journal International*, *206*, 1619–1633. <https://doi.org/10.1093/gji/ggw234>
- Wang, Y., Satake, K., Maeda, T., & Gusman, A. R. (2017). Green's function based tsunami data assimilation: A fast data assimilation approach toward tsunami early warning. *Geophysical Research Letters*, *44*, 10,282–10,289. <https://doi.org/10.1002/2017GL075307>
- Wessel, P., Smith, W. H. F., Scharroo, R., Luis, J. F., & Wobbe, F. (2013). Generic Mapping Tools: Improved version released. *Eos, Transactions American Geophysical Union*, *94*(45), 409–410. <https://doi.org/10.1002/2013EO450001>
- Yamamoto, N., Aoi, S., Hirata, K., Suzuki, W., Kunugi, T., & Nakamura, H. (2016). Multi-index method using offshore ocean-bottom pressure data for real-time tsunami forecast. *Earth, Planets and Space*, *68*(1), 128. <https://doi.org/10.1186/s40623-016-0500-7>
- Zhou, H., Wei, Y., & Titov, V. V. (2012). Dispersive modeling of the 2009 Samoa tsunami. *Geophysical Research Letters*, *39*, L16603. <https://doi.org/10.1029/2012GL053068>